




# Green synthesis of $\text{MnCr}_2\text{O}_4$ nanoparticles using *Vernonia amygdalina* (bitter leaf) for photocatalytic crystal violet dye degradation

Cyril O. Ugwuoke<sup>1,2</sup>, Abdudin G. Temam<sup>3,4</sup>, Rufus O. Ijeh<sup>5</sup>, Hope E. Nsude<sup>1</sup>, Ernest I. Ugwu<sup>1</sup>, Sylvester Mammah<sup>6</sup>, A. Agbogu<sup>1</sup>, Sabastine Ezugwu<sup>1,7</sup>, and Fabian I. Ezema<sup>1,8,9,10,\*</sup> 

<sup>1</sup> Department of Physics and Astronomy, University of Nigeria, Nsukka, Enugu State, Nigeria

<sup>2</sup> Science and Engineering Unit, Nigerian Young Researchers Academy, Onitsha, Anambra State 430231, Nigeria

<sup>3</sup> Department of Pure and Industrial Chemistry, University of Nigeria, Nsukka, Enugu State, Nigeria

<sup>4</sup> Department of Chemistry, Hawassa University, Hawassa, Ethiopia

<sup>5</sup> Science Education Department, College of Education, Agbor, Nigeria

<sup>6</sup> Department of Science Laboratory Technology, School of Applied Sciences, Rivers State Polytechnic Bori, Bori, Nigeria

<sup>7</sup> Dept. of Physics & Astronomy, University of Western Ontario, 1151 Richmond St, London, ON N6A 3K7, Canada

<sup>8</sup> Western Cape Province, Nanosciences African Network (NANOAFNET) iThemba LABS-National Research Foundation, 1 Old Faure Road, Somerset West 7129, Somerset West, Johannesburg, South Africa

<sup>9</sup> College of Graduate Studies, UNESCO-UNISA Africa Chair in Nanosciences/Nanotechnology, University of South Africa (UNISA), P.O. Box 392, Muckleneuk Ridge, Pretoria, South Africa

<sup>10</sup> Africa Centre of Excellence for Sustainable Power and Energy Development (ACE-SPED), University of Nigeria, Nsukka, Nigeria

**Received:** 6 April 2023

**Accepted:** 17 October 2023

**Published online:**  
7 November 2023

© The Author(s), under exclusive licence to Springer Science+Business Media, LLC, part of Springer Nature, 2023

## ABSTRACT

Various environmental concerns have emerged today as a result of the developing industrial revolution. The use of hazardous oxidizing agents and organic dyes is one of the biggest problems facing the textile industry today. This approach needs effective and affordable system to degrade such organic pollutants from the point sources. In this work,  $\text{MnCr}_2\text{O}_4$  nanoparticle is synthesized using a green method for a crystal violet dye removal from wastewater. Three nanoparticle samples (CMO-A, CMO-B and CMO-C) were synthesized via green synthesis using bitter leaf extract and different concentration (0.3 M, 0.4 M, and 0.5 M) of  $\text{KMnO}_4$ . The structural, morphological, optical properties, and photocatalytic activity of the synthesized  $\text{MnCr}_2\text{O}_4$  spinel were studied. X-ray diffraction (XRD) was used to examine the crystal structure and the  $\text{MnCr}_2\text{O}_4$  spinel exhibits cubic symmetry (Fd3m). The lattice parameters, crystallite size, microstrain, and dislocation density of the produced nanoparticles were also assessed using the diffraction data. The bandgap energy of the  $\text{MnCr}_2\text{O}_4$  spinel decreased from 1.96 to 1.81 eV as the concentration of Mn ion increases from 0.3 to 0.5 M. The  $\text{MnCr}_2\text{O}_4$  spinel

Address correspondence to E-mail: fabian.ezema@unn.edu.ng

showed good absorbance of light in visible range and also showed excellent photodegradation of crystal violet dye solution, with a record of 62.6%, 68.4%, and 74.9% degradation efficiency for CMO-A, CMO-B, and CMO-C, respectively, after 130 min of irradiation time.

## 1 Introduction

Today, several environmental challenges have arisen as a result of expanding industrial revolution to meet the demands of the global population whose number is growing rapidly [1, 2]. Among the various established industries, textile industries use different hazardous oxidizing agents and organic dyes for colouration and bleaching. Organic dyes were used by more than 50% of various colouring industries due to their stability and versatility compared to other dyes [3]. Particularly, effluents from textile industries and petroleum refineries released to rivers, lakes, and seawaters contain organic dyes, which are potentially cytotoxic, persistent, and mutagenic, and cause severe health issues to living organisms. Therefore, it is necessary to remove organic dyes from wastewater before releasing it into freshwater bodies. Unfortunately, most of these textile industries dump such dye containing organic wastes in rivers without doing appropriate treatment [4, 5]. As a result, the hazardous chemicals found in textile industry effluents can have a negative impact on water quality and pose a very harmful effects on animals when digested.

In the last three decades, the contaminated environments caused by excessive use of hydrocarbon-based resource buried deep inside the earth has sparked a debate among researchers about meeting the growing need for clean energy and clean water [6, 7]. As a result, various chemical, biological, and physical methods including membrane separation, adsorption, and coagulation were employed for dye or organic pollutants removal from wastewater [8]. However, these processes are not cost effective and only convert the liquid pollutants into solid form of sludge or membrane fouling [1, 9]. These water treatment procedures are confined to recovering organic waste from the liquid to solid phases of water which can be secondary pollutant [10]. Recently, photocatalysis has received a significant attention for removal of organic dyes. This process generates hydroxyl radicals ( $\cdot\text{OH}$ ) which are strong oxidants

to degrade the organic dyes [11, 12]. Currently, semiconductor metal oxide photocatalyst such as  $\text{TiO}_2$ ,  $\text{MnO}_2$ ,  $\text{Cr}_2\text{O}_3$ , has been produced, and substantial studies have been conducted to fully understand their potential in the breakdown of the organic dye, most especially those that can be easily biodegradable [13–15]. Moreover, the use of these semiconductor metal oxides in supercapacitors, sensors, solar cells, antibacterial activities etc. [16–20] has made the researchers understand the full concept of the faradaic processes in them. This has tremendously helped in achieving clean energy and organic waste control [21].

Among different metal oxides studied so far, titanium dioxide ( $\text{TiO}_2$ ) is widely used as a standard photocatalyst in degradation of organic dyes because of its excellent set of optical, physical, chemical, and electronic properties [19–25]. Also, it is low cost, eco-friendly, and possess a high chemical stability [26, 27]. Despite its benefits,  $\text{TiO}_2$  has a large band gap energy and electron-hole pair recombination, which are significant limitations that hinder its ability to perform photocatalysis and explain its poor visible light absorption [28]. This reduces its effectiveness in the degradation of organic waste when using visible light irradiation. Several modifications have been employed to curb this effect but these modifications necessitate additional cost, limiting the use of  $\text{TiO}_2$  as a photocatalyst. Many researchers have been in search of alternative semiconductor metal oxides with similar properties to  $\text{TiO}_2$ . To this end, chromium oxide ( $\text{Cr}_x\text{O}_y$ ) serves as an alternative material with an additional feature of variable oxidation state [29–31] [2]. The properties of chromium oxide have been enhanced by different modification techniques [31–33]. Chromium oxides and its spinel has been reported to be used in solar cell, catalysis, and spintronic applications [34–36].

The spinel is mostly preferred because it offers a better sintering reactivity. A few studies have been successfully reported on the metal doped  $\text{Cr}_x\text{O}_y$  or spinel. The spinel structure has the general formula  $\text{XY}_2\text{O}_4$  and uses cation distribution at two separate sites (X- and Y-). In this structure, divalent X (II) ions occupy

the tetrahedral gaps, while trivalent Y (III) ions fill the octahedral spaces in the compact packed arrangement of oxygen ions. Stüsser et al., used neutron diffraction technique to study the magnetic properties of  $\text{Cu}_{0.9}\text{Ni}_{0.1}\text{Cr}_2\text{O}_4$  and  $\text{CuCr}_2\text{O}_4$  and observed that the magnetic property of  $\text{ACr}_2\text{O}_4$  is greatly affected by the electronic property of A and Cr cations. They have reported ferromagnetic  $\text{Cu}_{0.9}\text{Ni}_{0.1}\text{Cr}_2\text{O}_4$  spinel [37]. Singh et al. have reported the optical properties of Mg ion substituted in  $\text{Cr}_{2-x}\text{Mg}_x\text{O}_3$ . They noted that the optical band gap reduced from 3 to 2.76 eV as the concentration of the magnesium ion increased [38].

Herein,  $\text{MnCr}_2\text{O}_4$  nanoparticles were synthesized via the green synthesis route using *Vernonia amygdalina* (bitter leaf) extract since the green method is inexpensive and environmentally friendly [39, 40]. The as-synthesized  $\text{MnCr}_2\text{O}_4$  nanoparticles were used as a photocatalyst for degradation of crystal violet from synthetic dye solution. To the best of our knowledge there is no reported work on the green synthesis of  $\text{MnCr}_2\text{O}_4$  spinel using bitter leaf extract and its application for dye degradation. This study provided a baseline idea for researchers and industries to extend the scope of their studies on organic pollutants treatment before discharging them to the environment.

## 2 Experimental

### 2.1 Preparation of *Vernonia amygdalina* leaf extract

The fresh leaves of *Vernonia amygdalina* (bitter leaf) were collected from the plant farm inside UNN, Nigeria and cleaned very well with distilled water, and dried for three days at room temperature. The dried leaves were blended. The mixture of *Vernonia amygdalina* (1 g) and distilled water (100 ml) was added to a beaker and stirred for 30 min while keeping the temperature at 60 °C. The resultant solution was sieved

and filtered to get a clear *Vernonia amygdalina* extract solution.

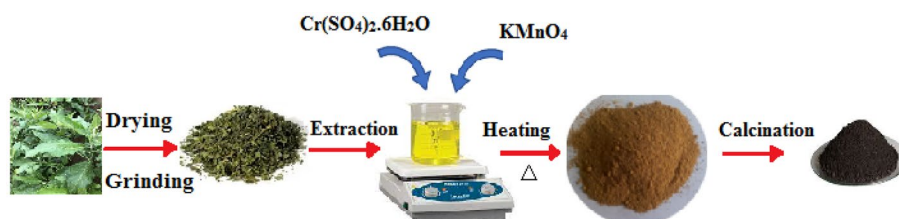
### 2.2 Synthesis of $\text{MnCr}_2\text{O}_4$ nanoparticles

The  $\text{MnCr}_2\text{O}_4$  nanoparticles was prepared using a green synthesis route shown in Fig. 1. In detail, 0.1 M of chromium sulphate hexahydrate ( $\text{Cr}(\text{SO}_4)_3 \cdot 6\text{H}_2\text{O}$ ) was prepared in 50 ml of bitter leaf extract, stirred with a magnetic stirrer and heated at the temperature of 60 °C for 10 min. 0.3 M of potassium permanganate ( $\text{KMnO}_4$ ) was added to the solution. As in Figure S1 in the Supplementary Information, upon addition of  $\text{KMnO}_4$ , the solution changed from brownish to deep purple colour, synonymous to slow release of Mn ions in the solution. This is followed by continuous heating (at 60 °C) and stirring until the solution turns to gel. The resultant mixture was centrifuged to collect the target sample and washed with distilled water three times to remove impurities and oven-dried overnight. After that, the sample was annealed at 500 °C for 2 h. and labelled as CMO-A. For comparison, CMO-B and CMO-C spinel samples were synthesized using the same procedure using 0.4 M and 0.5 M of  $\text{KMnO}_4$ , respectively.

### 2.3 Photocatalysis experiment

10 ppm of synthetic crystal violet dye solution was prepared carefully and stirred gently at room temperature for 50 min. The stock was prepared by adding 10 mg of CMO-A, CMO-B, and CMO-C each in 50 ml of crystal violet dye solution in a separate beaker and stirred in the dark for 50 min. This initiates the surface adsorption and desorption of crystal violet dye. Each of the beakers containing the mixture were exposed to sunlight and concentration of the dye was measured at every 10 min interval using double beam UV-Vis spectrophotometer. Photodegradation

**Fig. 1** Green synthesis process of  $\text{MnCr}_2\text{O}_4$  nanoparticle using bitter leaf extract



efficiency of the samples was calculated using Eq. 1; [41–44].

$$\text{Degradation efficiency} = \frac{C_o - C}{C_o} \times 100, \quad (1)$$

where  $C_o$  is initial concentration of the dye and  $C$  is concentration of the dye after degradation.

## 2.4 Characterization of the synthesized $\text{MnCr}_2\text{O}_4$ nanoparticles

The crystallographic structure and average crystal size of the  $\text{MnCr}_2\text{O}_4$  nanoparticles were characterized through X-ray diffraction (XRD) using a Bruker AXS D8 diffractometer (Bruker, Massachusetts, USA) connected to a copper anode at an incident wavelength of 1.540 Å. The crystal size of the nanoparticles were calculated using the Debye's Scherer's equation ( $D = (k\lambda/\beta \cdot \cos \theta)$ ) where  $D$  is crystal size,  $K$  is Scherer's constant (0.94),  $\lambda$  is the X-ray wavelength,  $\beta$  is full width at half maximum of the diffraction peak, and  $\theta$  is diffraction angle. The morphology and elemental composition of the  $\text{MnCr}_2\text{O}_4$  nanoparticles were studied by using a high resolution Tecnai F20 operating at 200 kV and equipped with an energy dispersive X-Ray spectroscopy (EDS) coupled to the scanning electron microscope (SEM). The absorbance peak of  $\text{MnCr}_2\text{O}_4$  nanoparticles were determined by using a double beam UV–Vis spectrophotometer.

## 3 Results and discussions

### 3.1 Characterization of synthesized $\text{MnCr}_2\text{O}_4$ nanoparticles

#### 3.1.1 X-ray diffraction characterization

The crystallographic structure and average crystal size of the  $\text{MnCr}_2\text{O}_4$  nanoparticles were determined using X-ray diffraction (XRD). The XRD pattern of the synthesized nanoparticles is shown in Fig. 2. It is noted that  $\text{MnCr}_2\text{O}_4$  has diffraction peaks at (111), (220), (222), (400), (331), (422), (440), (442), (620), (622), and (444) planes with the corresponding  $2\theta$  at (18.20°), (29.93°), (36.87°), (42.84°), (46.90°), (53.14°), (62.19°), (66.43°), (70.54°), (74.55°), and (78.48°), respectively. These planes indicate the formation of  $\text{MnCr}_2\text{O}_4$  at the right proportion having a structural formation of spinel cubic symmetry (Fd3m) [45, 46]. The formed

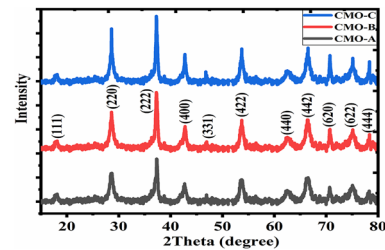


**Fig. 2** The XRD plot of the green route synthesized  $\text{MnCr}_2\text{O}_4$  nanoparticles

**Table 1** The composition of the  $\text{MnCr}_2\text{O}_4$

Sample	Crystallite size (nm)	Micro strain ( $\epsilon$ )	Dislocation density ( $\delta$ )	FWHM
CMO-A	16.78	0.0065	$3.55 \times 10^{-5}$	0.49929
CMO-B	17.61	0.0062	$3.22 \times 10^{-5}$	0.47566
CMO-C	17.90	0.0060	$3.12 \times 10^{-5}$	0.46801

$\text{MnCr}_2\text{O}_4$  has a face-centred cubic structure with JCPDS Card No. 01-075-1614. The average crystallite size, dislocation density, and microstrain of the synthesized nanoparticles are calculated using the relation [47–49].

$$D = \frac{k\lambda}{\beta \cos \theta} \quad (2)$$

$$\delta = 1/D^2 \quad (3)$$

$$\epsilon = \frac{\beta}{4 \tan \theta'} \quad (4)$$

where  $\delta$  is the dislocation density,  $\epsilon$  is the microstrain,  $\theta$  is the Bragg angle,  $\beta$  is FWHM,  $K = 0.94$ ,  $\lambda$  is the wavelength of X-ray,  $D$  is the crystallite size.

The tensile strain and comprehensive stress of the formed nanoparticle is depicted by the positive and negative values of  $\epsilon$ , respectively, whereas its defect is represented by  $\delta$ . Table 1 shows the crystallite size, microstrain and dislocation density of the nanoparticles. The crystallite size for CMO-A, CMO-B and CMO-C are 16.78, 17.61, and 17.90 nm, respectively. The result show that there is an increase in the crystallite size of the obtained nanoparticles as a result of the increasing the molar concentration of  $\text{KMnO}_4$  which is a precursor solution for Mn. The defect in the formed nanoparticles was observed to be low as indicated in Table 1. The tensile stress of CMO-B and CMO-A were observed to be high, whereas CMO-C

shows the lowest tensile stress. The low dislocation density and low strain shown by CMO-C could be due to the proper insertion of  $\text{Mn}^{2+}$  into the structure of  $\text{Cr}_x\text{O}_y$ . This result is in agreement with the works of Hamza et al. [50].

XRD analyses were also performed on two control samples: (a) sample synthesized without the addition of bitter leaf extract (but annealed at  $500\text{ }^\circ\text{C}/2\text{ h}$ ), and (b) sample grown in the same condition as CMO-A, but without calcination at  $500\text{ }^\circ\text{C}$ . The result of the XRD measurements is shown in Figure S2 in the supplementary information. A few matching peaks at (111), (220), and (442) can be identified in the XRD profile of the sample synthesized using our green route (i.e., using bitter leaf extract) but without calcination. For this sample, the XRD pattern did not show a clear, distinct, and sharp diffraction peak for each different phase, which strongly suggests that the sample is mostly amorphous. This is a confirmation that high-temperature annealing at  $500\text{ }^\circ\text{C}$  is a necessary condition for the formation of  $\text{MnCr}_2\text{O}_4$  polycrystalline NP as shown in Fig. 2; Table 1 above. The XRD of the sample prepared without bitter leaf extract, though showed some well-defined peaks, none of such peaks match the peaks shown in Fig. 1. The sample is therefore not the same as  $\text{MnCr}_2\text{O}_4$ . Going by the results above, we can affirm that the use of bitter leaf extract, followed by a high-temperature

annealing are the necessary conditions to synthesize polycrystalline  $\text{MnCr}_2\text{O}_4$  reported in this paper.

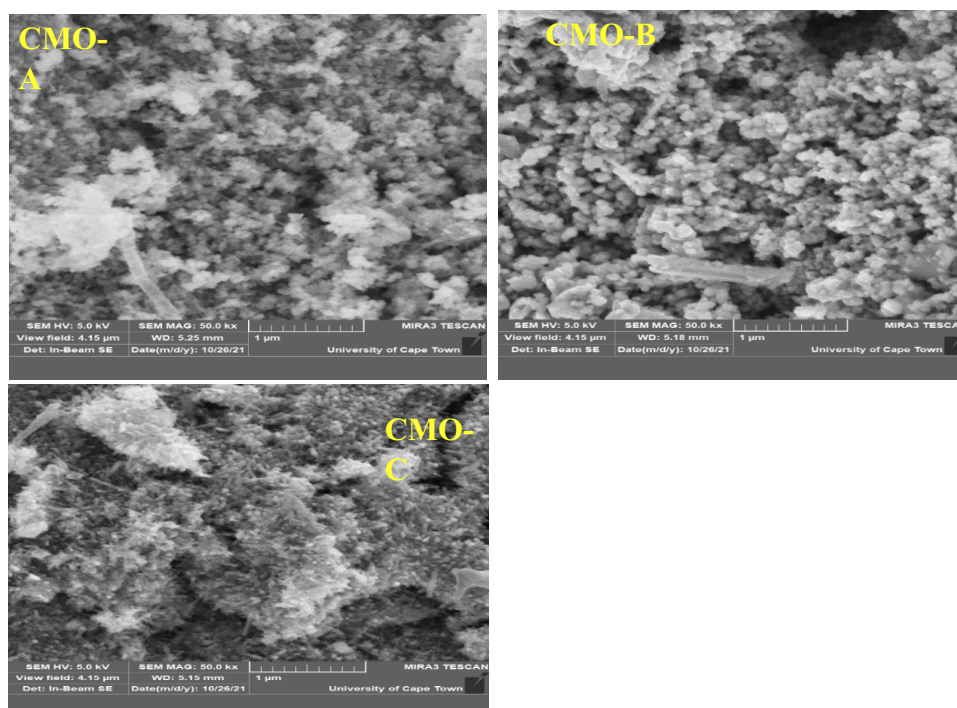
### 3.1.2 Scanning electron microscope (SEM) characterization

A scanning electron microscope was used to analyze the morphology of the synthesized nanoparticles [51]. As displayed in Fig. 3, the SEM image for all of the  $\text{MnCr}_2\text{O}_4$  nanoparticle samples reveal the surface morphology of the samples and clearly show the effect of a varying precursor concentration. The CMO-A has clustered irregular spherical shape, whereas CMO-B and CMO-C appear to have small densely packed nanospherical shapes. The micrograph confirms that the change in precursor concentration alters the surface morphology of the samples. Figure 3a, b and c show the SEM images of  $\text{MnCr}_2\text{O}_4$  nanoparticle synthesized using 0.3, 0.4 and 0.5 M of  $\text{KMnO}_4$  as a Mn precursor, respectively.

### 3.1.3 Energy Dispersive X-ray (EDX) characterization

Energy Dispersive X-ray (JEOL-IT300 LA) analysis was used for determining the elemental composition of the synthesized  $\text{MnCr}_2\text{O}_4$  nanoparticles. Energy dispersive X-ray (EDX) analysis is a technique for

**Fig. 3** SEM micrograph for surface morphology analysis of the  $\text{MnCr}_2\text{O}_4$  nanoparticles



elemental and compositional analysis based on the information from the X-rays produced by electron irradiation. Once a vacancy is created in the electron orbital of the inner shell of a constituent atom by an incident electron, electrons with a higher electron level are transferred from the outer shell to stabilize it. In other words, the high energy primary electron beam causes emission of an inner shell electron which leaves the atom in an excited state. The presence of  $\text{MnCr}_2\text{O}_4$  is evidenced by the EDX shown in Fig. 4. The samples have traces of impurities such as sulphur, phosphorous, potassium, and carbon. These impurities demonstrated that the green extract phytochemicals are involved in both capping and reduction of the formed nanoparticles. This assertion is confirmed by Alara et al. [52]. They studied the EDS of bitter leaf extract and it was noted that bitter leaf has a high content of

oxygen and carbon and moderate potassium, phosphorous, and silicon. Therefore, the traces of these impurities in the EDX spectra suggest the existence of the stabilizing agents [53].

### 3.2 Optical properties study

The absorbance of  $\text{MnCr}_2\text{O}_4$  was studied within 300 to 1000 nm spectra range using UV–vis spectroscopy. Figure 5a shows the absorbance of  $\text{MnCr}_2\text{O}_4$  at various precursor concentrations. It was observed that the increase in wavelength causes the absorbance of manganese chromium oxide to decrease. The absorbance peaks were recorded to be 0.59, 0.61, and 0.62 for CMO-A, CMO-B, and CMO-C, respectively. This result is in consensus with the works of Dumitru et al. [54], which supports the notion that

**Fig. 4** The Energy dispersive X-ray (EDX) spectra for elemental analysis of  $\text{MnCr}_2\text{O}_4$  nanoparticles

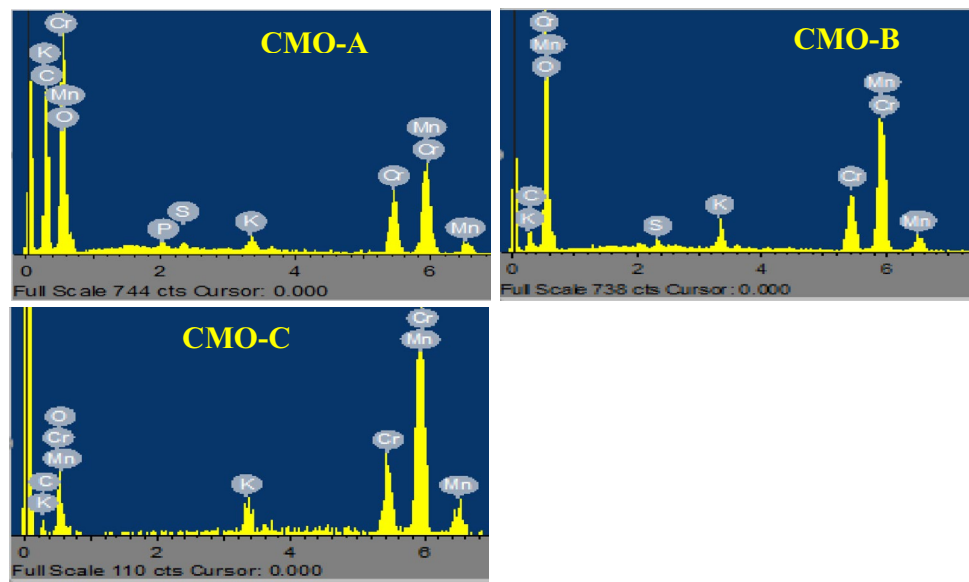
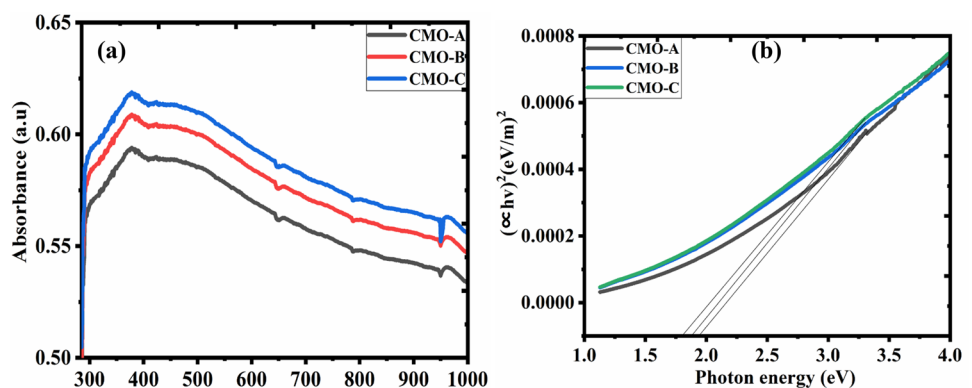


**Fig. 5** The absorbance spectra **a** and optical bandgap pointing plot **b** of  $\text{MnCr}_2\text{O}_4$



the absorbance of spinel decreases with an increase in wavelength. They observed that  $\text{ZnCr}_2\text{O}_4$  has a broad peak of absorbance from 200 to 650 nm wavelength range, which is comparable with the  $\text{MnCr}_2\text{O}_4$  250 to 700 nm wavelength broad peak of absorbance shown in Fig. 5a.

The measure of the absorption coefficient in relation to photon energy ( $h\nu$ ) determines the energy bandgap. The optical band gap of  $\text{MnCr}_2\text{O}_4$  is defined by the Equation [55, 56].

$$(\alpha h\nu)^{\frac{1}{2}} = A(h\nu - E_g), \quad (5)$$

where  $A$  is a proportionality constant,  $\alpha$  is the absorption coefficient and constant  $E_g$  is the energy bandgap. The energy band gap of  $\text{MnCr}_2\text{O}_4$  is determined by plotting the absorption coefficient against photon energy. The energy band gap plot of  $\text{MnCr}_2\text{O}_4$  is shown in Fig. 5b. The plot revealed that the energy band gap decreases as the precursor concentration increases. It was noted that the optical band gap for CMO-A, CMO-B and CMO-C are 1.96, 1.89, and 1.81 eV, respectively. This result is in harmony with the works of Jafarnejad et al. [57], who reported the optical band gap of  $\text{MnCr}_2\text{O}_4$  in nanoparticle and bulk form to be 1.8 eV and 1.4 eV, respectively.

### 3.3 Photocatalytic activity

The electron-hole pairs generated during the excitation of electrons when photo-irradiated usually facilitate the degradation of crystal violet dye. Photocatalysts with excellent surface adsorption aid the degradation process [58]. In this work, the photodegradation experiment of crystal violet dye was examined using sunlight as the irradiation source. At every 10 min interval, we recorded the absorption spectrum of each sample. Figure 6a show the photodegradation of crystal violet dye using  $\text{MnCr}_2\text{O}_4$ . It was observed that all the samples showed positive degradation upon irradiation of sunlight and this leads to the colour change of the solution within the exposure time (0–130 min) as presented in Fig. 6d. CMO-C showed excellent degradation compared to CMO-A and CMO-B. After 130 min, the photodegradation efficiency of CMO-A, CMO-B, and CMO-C was calculated to be 62.6%, 68.4%, and 74.9%, respectively (see Fig. 7a). CMO-A showed the least degradation, this could be the effect of the high trace of impurities and low value of crystallite size. This finding is in line with the findings of Hamza et al., who used  $\text{Mn}_x\text{Cr}_y\text{O}_2$  to photodegrade alizarin red [50]. After 180 min, they found a deterioration efficiency of up to 88.9%. The results are

**Fig. 6** Photodegradation of crystal violet dye using  $\text{MnCr}_2\text{O}_4$  spinels at different-time and the rate of colour changes after photodegradation

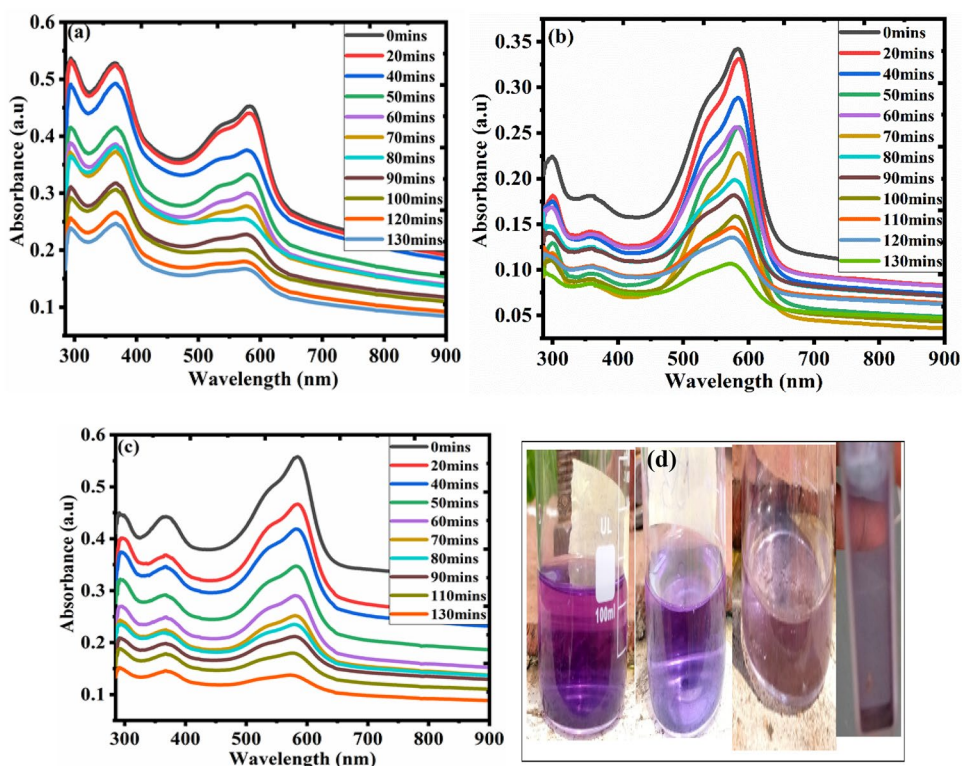
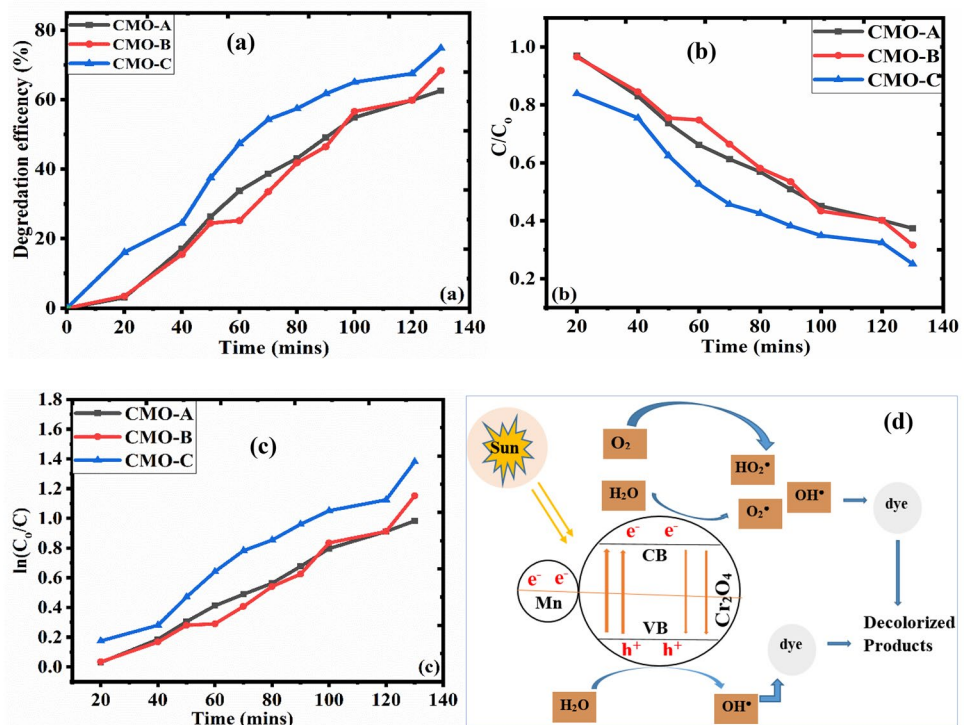


**Fig. 7** The plot of photo-degradation efficiency **a**,  $C/C_0$  versus time **b**, variation of  $\ln(C_0/C)$  with respect to time **c**, and photocatalytic mechanism **d**, of crystal violet degradation using  $MnCr_2O_4$  nanoparticles



similarly consistent with the findings of Dumitru et al., who have reported a 60% photodegradation efficiency for  $ZnCr_2O_4$  against humic acid after 3 h [54].

The variation of  $\ln(C_0/C)$  with respect to time shown in Fig. 7c was used to determine the reaction kinetics of the experiments. The nanoparticles with a high value of reaction kinetic constant offer a better photodegradation of organic dye. Table 2 shows the correlation coefficient ( $R^2$ ), kinetic rate constant, photodegradation efficiency and the energy bandgap of  $MnCr_2O_4$  nanoparticles. From the table, the reaction kinetics and correlation coefficient of CMO-A, CMO-B, and CMO-C was observed to be  $8.89 \times 10^{-3}$ ,  $1.01 \times 10^{-3}$ ,  $10.78 \times 10^{-3} \text{ min}^{-1}$ , and 0.9934, 0.9612, 0.9679, respectively. CMO-C has the highest value reaction kinetics constant and the lowest correlation coefficient; this justifies the 74.9% of photodegradation efficiency achieved. The rate of photodegradation of crystal

violet dye by  $MnCr_2O_4$  nanoparticles was determined using the pseudo first-order kinetics [59].

$$\ln C = -kt + \ln C_0 \quad (6)$$

$$\ln \frac{C_0}{C} = kt, \quad (7)$$

where  $t$  is the exposure time and  $k$  is the reaction kinetics constant.

The contact time required to achieve equilibrium is proportional to the initial dye concentration. Figure 7a–c provides an illustration of how contact time affects the degradation of crystal violet. The catalyst can be recycled completely through physical method which is filtration and then thermal treatments. The proportion of crystal violet degradation is evidently increasing with extended contact time, as shown in Fig. 7a. This results mostly from the method by which

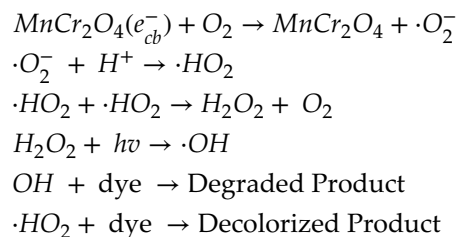
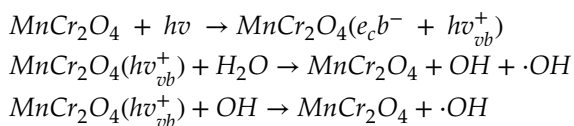
**Table 2** Summary on photocatalytic degradation of crystal violet using  $MnCr_2O_4$  nanoparticles

Sample	Correlation coefficient ( $R^2$ )	kinetic rate constant $K$ ( $\text{min}^{-1}$ )	Photodegradation efficiency (%) at 130 min	Energy bandgap (eV)
CMO-A	0.9934	$8.89 \times 10^{-3}$	62.6	1.96
CMO-B	0.9612	$1.01 \times 10^{-3}$	68.4	1.89
CMO-C	0.9679	$10.78 \times 10^{-3}$	74.9	1.81



the dye molecules adhere to the nanoparticle's surface and the adsorption sites became more and more loaded as the contact time increased. Table 3 summarizes the photodegradation of various organic dyes using different chromium spinel. It is observed that the percentage of dye degradation of the synthesized  $MnCr_2O_4$  nanoparticle is comparable with that of other spinel summarized in Table 3, while the quantity of photocatalyst used in this work is far smaller, making it cost effective.

Moreover, the photocatalytic degradation mechanism of crystal violet dye using  $MnCr_2O_4$  can take place following four major steps as shown in Fig. 7d [60]; (i) The diffusion of the dye molecules from the contaminated water to the surface of  $MnCr_2O_4$ , (ii) The surface adsorption of crystal violet dye, (iii) Chains of oxidation/reduction reaction processes at the adsorbed surfaces and (iv) The desorption of crystal violet dye at  $MnCr_2O_4$  surface. The purpose of desorption is to liberate the surface of the spinel photocatalyst for new reactant adsorption [61]. The stability and low interfacial charge recombination at the surface of  $MnCr_2O_4$  create room for the reaction between the oxidant and electrons, and the reductant and holes [62]. The OH and  $H_2O$  are oxidized by the holes to form  $\cdot OH$ . Similarly,  $O_2$  is reduced by the electrons to form  $\cdot O_2^-$  (superoxide radical anions). The  $H^+$  in water protonates  $\cdot O_2^-$  to form  $HO_2^-$  (hydroperoxide radical), this peroxide radical subsequently becomes  $H_2O_2$  [63]. The  $H_2O_2$  is later disassociated forming  $\cdot OH$ . The formed  $\cdot HO_2^-$  and  $\cdot OH$  are very effective in the degradation of crystal violet dye [64, 65]. The degradation processes can be summarized as.



## 4 Conclusion

We investigated the influence of Mn concentration in the structural, morphological, optical, and photocatalysis behaviour of  $MnCr_2O_4$ .  $MnCr_2O_4$  spinel was synthesized using green synthesis route. *Vernonia amygdalina* (bitter leaf), was used as the green extract. The Mn precursor concentrations were varied between 0.3, 0.4 and 0.5 M. The XRD result of  $MnCr_2O_4$  spinel synthesized at 0.5 M has low dislocation strength, good tensile strength and high crystallite size when compared to other concentrations. The optical studies confirmed excellent absorbance and the energy band-gap for synthesized  $MnCr_2O_4$  spinels are 1.96, 1.89, and 1.81 eV for CMO-A, CMO-B and CMO-C, respectively.  $MnCr_2O_4$  spinel showed a positive response to the photodegradation of crystal violet dye. The degradation efficiency was recorded to be 62.6%, 68.4%, and 74.9% degradation efficiency for CMO-A, CMO-B, and CMO-C, respectively. The reaction kinetics and correlation coefficient  $8.89 \times 10^{-3}$ ,  $1.01 \times 10^{-3}$ ,  $10.78 \times 10^{-3} \text{ min}^{-1}$ , and 0.9934, 0.9612, 0.9679 were recorded for CMO-A, CMO-B, and CMO-C, respectively. The synthesized  $MnCr_2O_4$  nanoparticle shows a good photocatalytic activity to degrade crystal violet. Finally, we recommend that any interested researcher can do

**Table 3** Comparison on chromium spinels photocatalyst performance for different organic dyes

Photocatalyst	Photocatalyst quantity (mg)	Dye	Percentage degradation (%)	Degradation time (mins)	Ref.
$CuCr_2O_4$	20	Methylene blue	99.5	60	[66]
$CoCr_2O_4$	40	Eriochrome BlackT (EBT)	90	90	[67]
$CuCr_2O_4$	100	Azo dyes	99.6	120	[68]
$CuCr_2O_4$	40	Monoazo dye (AV 7)	68.2	120	[69]
$BiVO_4/CuCr_2O_4/PANI$	10	Methylene blue	95	180	[70]
$MnxCr_yO_2$	40	Alizarin red	88.9	180	[50]
$MnCr_2O_4$	10	Crystal violet	74.9	130	This work

further investigation on this catalyst for other dyes as well as a real sample discharged from industries.

### Authors contributions

COU carried out the experimental work and drafted the manuscript. AGT revised the manuscript. ROI and HEN analyze experimental result. EIU, SM and AA read the approved submitted manuscript. SE, FIE supervised the project. All authors read and approved the final manuscript.

### Funding

FIE acknowledges the grant by TETFUND under contract number.

TETFUND/DR&D/CE/UNI/NSUKKA/RP/VOL.I and also acknowledges the support received from the Africa Centre of Excellence for Sustainable Power and Energy Development (ACE-SPED), University of Nigeria, Nsukka. We thank Engr. Emeka Okwuosa for the generous sponsorship of April 2014, July 2016, July 2018, and July 2021 conferences/workshops on applications of nanotechnology to energy, health & Environment and for providing some research facilities.

### Data availability

The data that support the findings of this research work are available from the corresponding author upon reasonable request.

### Declarations

**Competing interests** The authors declare that they have no conflict of interest.

**Supplementary information** The online version contains supplementary material available at <https://doi.org/10.1007/s10854-023-11499-z>.

### References

1. S. Aman, S. Gouadria, F.F. Alharbi et al., Novel Sr-based  $\text{Al}_2\text{O}_4$  spinel material an environmental friendly electrode for supercapacitor application. *Appl. Phys. A* **129**, 347 (2023). <https://doi.org/10.1007/s00339-023-06591-4>
2. M. Waheed, K. Jabbour, S. Houda, F.M.A. Alzahrani, K.M. Katubi, S. Riaz, M.S. Al-Buriah, Fabrication of mesoporous Er doped  $\text{ZnMnO}_3$  nanoflake via sol gel approach for energy storage application. *Ceram. Int.* (2023). <https://doi.org/10.1016/j.ceramint.2022.11.328>
3. M. Abudllah, M. Al Huwayz, N. Alwadai et al., Facile fabrication of ternary  $\text{CuO/CuS/ZnS}$  for photodegradation of methylene blue. *J. Korean Ceram. Soc.* **60**, 569–580 (2023). <https://doi.org/10.1007/s43207-023-00287-4>
4. O.S. Okwundu et al., Heavy metal sorption using thiolated oils of *elaeis guineensis* and *glycine max*. *Metall. Mater. Eng.* **26**(3), 317–327 (2020). <https://doi.org/10.30544/538.5>
5. R. Yang et al.,  $\text{MnO}_2$ -Based materials for environmental applications. *Adv. Mater.* **33**(9), 1–53 (2021). <https://doi.org/10.1002/adma.202004862>
6. O.S. Okwundu, C.O. Ugwuoke, A.C. Okaro, Recent trends in non-faradaic Supercapacitor Electrode materials. *Metall. Mater. Eng.* **25**, 105–138 (2019). <https://doi.org/10.30544/417>
7. C.O. Ugwuoke, S. Ezugwu, S.L. Mammah, A.B.C. Ekwealor, F.I. Ezema, The Application of carbon and graphene quantum dots to emerging optoelectronic devices, in *Electrode materials in energy storage and conversion*. (Taylor & Francis, UK, 2021), pp.421–436. <https://doi.org/10.1201/9781003145585-22>
8. I.K. Konstantinou, T.A. Albanis,  $\text{TiO}_2$ -assisted photocatalytic degradation of azo dyes in aqueous solution: kinetic and mechanistic investigations: a review. *Appl. Catal. B Environ.* **49**(1), 1–14 (2004). <https://doi.org/10.1016/j.apcatb.2003.11.010>
9. V.S. Kirankumar, S. Sumathi, A review on photodegradation of organic pollutants using spinel oxide. *Mater. Today Chem.* **18**, 100355 (2020)
10. S. Guo, H. Lin, K. Zheng, Z. Xiao, F. and, Li, Sulfanilic acid-modified P25  $\text{TiO}_2$  nanoparticles with improved photocatalytic degradation on Congo Red under visible light. *Dye. Pigment.* no. **92**, 1278–1284 (2012). <https://doi.org/10.1016/j.dyepig.2011.09.004>
11. A.M. Alenad, M.S. Waheed, S. Aman, N. Ahmad, A.R. Khan, R.Y. Khosa, T.A.M. Taha, Visible light driven Ni doped hematite for photocatalytic reduction of noxious methylene blue. *Mater. Res. Bull.* **165**, 112306 (2023). <https://doi.org/10.1016/j.materresbull.2023.112306>

12. H.A. Alburaih, S. Aman, N. Ahmad, S.R. Ejaz, R.Y. Khosa, A.G. Abid, T.A. Taha, Synergistic photodegradation of methylene blue by Sm doped Fe<sub>2</sub>O<sub>3</sub> photocatalyst under sunlight. *Chin. J. Phys.* **83**, 637–649 (2023). <https://doi.org/10.1016/j.cjph.2022.08.017>
13. S. Das, A. Samanta, S. Jana, Light-assisted synthesis of hierarchical flower-Like MnO<sub>2</sub> nanocomposites with solar light induced enhanced photocatalytic activity. *ACS Sustain. Chem. Eng.* (2017). <https://doi.org/10.1021/acssuschemeng.7b02003>
14. H. Zhang et al., Visualization of the formation and 3D porous structure of Ag doped MnO<sub>2</sub> aerogel monoliths with high photocatalytic activity. *ACS Sustain. Chem. Eng.* (2016). <https://doi.org/10.1021/acssuschemeng.6b00578>
15. Y. Yang et al., UV-visible-infrared light-driven photothermocatalytic abatement of CO on Cu doped ramsdellite MnO<sub>2</sub> nanosheets enhanced by a photoactivation effect. *Applied Catal. B Environ.* (2017). <https://doi.org/10.1016/j.apcatb.2017.11.017>
16. C.O. Ugwuoke, P.C. Tagbo, O.S. Okwundu, C.A. Okaro, S. Ezugwu, F.I. Ezema, “Low-Temperature Processed Metal Oxides and Ion-Exchanging Surfaces as pH Sensor,” in *Chemically deposited nanocrystalline metal oxide thin films, synthesis, characterization, and applications*, 2021, pp. 821–861
17. S.O. Aisida et al., Biogenic synthesis of iron oxide nanorods using *Moringa oleifera* leaf extract for antibacterial applications. *Appl. Nanosci.* **10**, 305–315 (2020)
18. N. Madubuonua et al., Biosynthesis of iron oxide nanoparticles via a composite of Psidium guavaja-Moringa oleifera and their antibacterial and photocatalytic study. *J. Photochem. Photobiol B Biol.* **199**, 111601 (2019)
19. S.O. Aisida et al., Biogenic synthesis and antibacterial activity of controlled silver nanoparticles using an extract of Gongronema Latifolium. *Mater. Chem. Phys.* **237**, 121859 (2019)
20. C.A. Okaro, O.S. Okwundu, P.C. Tagbo, C.O. Ugwuoke, S. Ezugwu, F.I. Ezema, Nanostructured Metal Oxide-Based Electrode Materials for Ultracapacitors, in *Chemically Deposited Nanocrystalline Metal Oxide Thin Films*. (Springer Nature, Germany, 2021), pp.561–599. [https://doi.org/10.1007/978-3-030-68462-4\\_22](https://doi.org/10.1007/978-3-030-68462-4_22)
21. X. Hao et al., Mild aqueous synthesis of urchin-like MnOx hollow nanostructures and their properties for RhB degradation. *Chem. Eng. J.* (2013). <https://doi.org/10.1016/j.cej.2013.06.007>
22. R.T. Rasheed, H.S. Mansoor, R.R. Al-shaikhly, Synthesis and catalytic activity studies of  $\alpha$ -MnO<sub>2</sub> nanorodes, rutile TiO<sub>2</sub> and its composite prepared by hydrothermal method. *AIP Conference Proceedings* **2213**, 020122 (2020)
23. W.H. Kuan, C.Y. Chen, C.Y. Hu, Removal of methylene blue from water by  $\gamma$ -MnO<sub>2</sub>. *Water Sci. Technol.* (2011). <https://doi.org/10.2166/wst.2011.262>
24. P. Cui, Y. Chen, G. Chen, Degradation of low concentration methyl orange in aqueous solution through sonophotocatalysis with simultaneous recovery of photocatalyst by ceramic membrane microfiltration. *Industrial Eng. Chem. Res.* (2011). <https://doi.org/10.1021/ie100832q>
25. C. Hou, B. Hu, J. Zhu, Photocatalytic degradation of methylene blue over TiO<sub>2</sub> pretreated with varying concentrations of NaOH. *Catalysts* **8**, 575 (2018). <https://doi.org/10.3390/catal8120575>
26. M. Rai, C. Dos-Santos, *Nanotechnology Applied To Pharmaceutical Technology* (Springer, Switzerland, 2017)
27. A. Fujishima, X. Zhang, D.A. Tryk, TiO<sub>2</sub> photocatalysis and related surface phenomena. *Surf. Sci. Rep.* (2008). <https://doi.org/10.1016/j.surfrep.2008.10.001>
28. C.O. Ugwuoke, S. Ezugwu, S.L. Mammah, A.B.C. Ekwealor, M. Suguyima, F.I. Ezema, “Physical Methods to Fabricate TiO<sub>2</sub> QDs for Optoelectronics Applications,” in *Electrode materials in energy storage and conversion*, 2021, pp. 321–338. <https://doi.org/10.1201/9781003145585-15>
29. S. Chandrasekaran, C. Bowen, P. Zhang, Z. Li, Q. Yuan, X. Ren, L. Deng, Spinel photocatalysts for environmental remediation, hydrogen generation, CO<sub>2</sub> reduction and photoelectrochemical water splitting. *J. Mater. Chem. A* **6**, 11078–11104 (2018)
30. S.K. Rawal, R. Chandra, “Wettability And Optical Studies Of Films prepared from Power Variation Of Co-Sputtered Cr And Zr Targets By Sputtering,” in *2nd International Conference on Innovations in Automation and Mechatronics Engineering, ICIAME 2014*, 2014, vol. 14, pp. 304–311. <https://doi.org/10.1016/j.protcy.2014.08.040>
31. A. Zekaik, H. Benhebal, B. Benrabah, Synthesis and characterization of Cu doped chromium oxide (Cr<sub>2</sub>O<sub>3</sub>) thin films. *High Temp. Mater. Proc* **38**, 806–812 (2019)
32. J.T. Anandhi, S.L. Rayer, T. Chithambarathanu, F.T.I.R. “Synthesis, Studies, Optical properties of aluminium doped chromium oxide nanoparticles by microwave irradiation at different concentrations. *Chem. Mater. Eng.* **5**(2), 43–54 (2017). <https://doi.org/10.13189/cme.2017.050204>
33. J. Sackey, R. Morad, A.K.H. Bashir, L. Kotsedi, C. Kaonga, M. Maaza, Bio-synthesised black  $\alpha$ -Cr<sub>2</sub>O<sub>3</sub> nanoparticles; experimental analysis and density function theory calculations. *J. Alloys Compd.* **850**, 156671 (2021). <https://doi.org/10.1016/j.jallcom.2020.156671>
34. P. Mohanty, A.R.E. Prinsloo, B.P. Doyle, E. Carleschi, C.J. Sheppard, Structural and magnetic properties of (Co<sub>1-x</sub>Nix)

- Cr<sub>2</sub>O<sub>4</sub> (x = 0.5, 0.25) nanoparticles. AIP Adv. (2018). <https://doi.org/10.1063/1.5006568>
35. P. Mohanty, C.J. Sheppard, A.R.E. Prinsloo, Field induced magnetic properties of Ni doped CoCr<sub>2</sub>O<sub>4</sub>. AIP Adv. **2115**, 030195 (2019)
36. H. Mohamed et al., Comprehensive study on morphological, structural and optical properties of Cr<sub>2</sub>O<sub>3</sub> nanoparticle and its antibacterial activities. J. Mater. Sci. Mater. Electron. **0**(0), 0 (2019). <https://doi.org/10.1007/s10854-019-01125-2>
37. N. Stüsser, M. Reehuis, M. Tovar, B. Klemke, A. Hoser, J. Hoffmann, Spin reorientation by Ni doping in Cu<sub>1-x</sub>Nix-Cr<sub>2</sub>O<sub>4</sub> spinels with x = 0 and 0.1, and evidence for canted magnetic order above the onset of a ferromagnetic Cu. J. Magn. Magn. Mater. **506**, 166683 (2020). <https://doi.org/10.1016/j.jmmm.2020.166683>
38. J. Singh, V. Verma, R. Kumar, R. Kumar, Influence of Mg<sup>2+</sup>-substitution on the optical band gap energy of Cr<sub>2-x</sub>MgxO<sub>3</sub> nanoparticles. Results Phys. **13**, 102106 (2019). <https://doi.org/10.1016/j.rinp.2019.02.042>
39. N. Shinde, M. Lokhande, A. C., C.D. Lokhande, A green synthesis method for large area silver thin film containing nanoparticles. J. Photochem. Photobiol., B **136**, 19–25 (2014). <https://doi.org/10.1016/j.jphotobiol.2014.04.011>
40. N.M. Shinde, A.C. Lokhande, J.S. Bagi, C.D. Lokhande, Biosynthesis of large area (30×30 cm<sup>2</sup>) silver thin films. Mater. Sci. Semicond. Process. vol. **22**, 28–36 (2014). <https://doi.org/10.1016/j.mssp.2014.01.011>
41. T. Siyao, Y. Xiaocai, Y. Danni, W. Liping, L. Jiaqi, Z. Wanting, Study on degradation of diesel pollutants in seawater by composite photocatalyst MnO<sub>2</sub>/ZrO<sub>2</sub>. Water Sci. Technol. (2020). <https://doi.org/10.2166/wst.2020.316>
42. S. Zhou, Z. Du, X. Li, Y. Zhang, Degradation of methylene blue by natural manganese oxides: kinetics and transformation products. R Soc. Open. Sci. **6**, 190351 (2019). <https://doi.org/10.1098/rsos.190351>
43. D. Mondal, S. Das, B. Kumar, D. Bhattacharya, Size engineered Cu-doped α-MnO<sub>2</sub> nanoparticles for exaggerated photocatalytic activity and energy storage application. Mater. Res. Bull. (2019). <https://doi.org/10.1016/j.materresbull.2019.03.023>
44. M. Touqeer et al., New Co-MnO based Nanocrystallite for photocatalysis studies driven by visible light. J. Taibah Univ. Sci. (2020). <https://doi.org/10.1080/16583655.2020.1846966>
45. A. Afzal, S. Atiq, M. Saleem, S.M. Ramay, S. Naseem, S.A. Siddiqi, Structural and magnetic phase transition of sol-gel-synthesized Cr<sub>2</sub>O<sub>3</sub> and MnCr<sub>2</sub>O<sub>4</sub> nanoparticles. J. Sol-Gel Sci. Technol. **80**(1), 96–102 (2016). <https://doi.org/10.1007/s10971-016-4066-4>
46. E.T. Sibanda, A.R.E. Prinsloo, C.J. Sheppard, P. Mohanty, Size effect on magnetic properties of MnCr<sub>2</sub>O<sub>4</sub> nanoparticles. J. Magn. Magn. Mater. **558**, 169486 (2022). <https://doi.org/10.1016/j.jmmm.2022.169486>
47. N. Madubuonu et al., Bio-inspired iron oxide nanoparticles using Psidium guajava aqueous extract for antibacterial activity. Appl. Phys. A **126**(72), 1–8 (2020)
48. S.O. Aisida et al., Biosynthesis of silver oxide nanoparticles using leave extract of Telfairia Occidentalis and its antibacterial activity. Mater. Today Proc **36**, 208–213 (2021)
49. X. Zeng, B. Li, R. Liu, X. Li, T. Zhu, Investigation of promotion effect of Cu doped MnO<sub>2</sub> catalysts on ketone-type VOCs degradation in a one-stage plasma-catalysis system. Chem. Eng. J. (2019). <https://doi.org/10.1016/j.cej.2019.123362>
50. M. Hamza et al., Catalytic removal of alizarin red using chromium manganese oxide nanorods: degradation and kinetic studies. Catalysts. **10**, 1150 (2020). <https://doi.org/10.3390/catal10101150>
51. R.O. Ijeh, C.O. Ugwuoke, E.B. Ugwu, S.O. Aisida, F.I. Ezema, Structural, optical and magnetic properties of Cu-doped ZrO<sub>2</sub> films synthesized by electrodeposition method. Ceram. Int. **48**(4), 4686–4692 (2022). <https://doi.org/10.1016/j.ceramint.2021.11.004>
52. O.R. Alara, N.H. Abdurahman, C. Ishmael, N.A. Kabbashi, Extraction and characterization of bioactive compounds in *Vernonia amygdalina* leaf ethanolic extract comparing Soxhlet and microwave-assisted extraction techniques. J. Taibah Univ. Sci. **13**(1), 414–422 (2019). <https://doi.org/10.1080/16583655.2019.1582460>
53. N. Bala et al., Green Synthesis of zinc oxide nanoparticles using Hibiscus subdariffa leaf extract: effect of temperature on synthesis, anti-bacterial activity and antidiabetic activity. RSC Adv. **5**, 4993–5003 (2014)
54. R. Dumitru et al., “Synthesis, characterization of nanosized ZnCr<sub>2</sub>O<sub>4</sub> and its photocatalytic performance in the degradation of humic acid from drinking water. Catalysts (2018). <https://doi.org/10.3390/catal8050210>
55. M.M. Abdullah, F.M. Rajab, S.M. Al-Abbas, “Structural and optical characterization of Cr<sub>2</sub>O<sub>3</sub> nanostructures: Evaluation of its dielectric properties,” vol. 027121, no. October 2013, 2014, <https://doi.org/10.1063/1.4867012>
56. I.L. Ikhioya, C.O. Ugwuoke, R.M. Obodo, D.N. Okoli, M. Maaza, F.I. Ezema, Influence of precursor pH on Bi doped ZnSe material via electrochemical deposition technique.

- Appl. Surf. Adv. **9**, 100232 (2022). <https://doi.org/10.1016/j.apsadv.2022.100232>
57. E. Jafarnejad, S. Khanahmadzadeh, F. Ghanbary, M. Enhesari, Synthesis, characterization and optical band gap of Pirochromite ( $\text{MgCr}_2\text{O}_4$ ) nanoparticles by Stearic Acid Sol-Gel Method. *Curr. Chem. Lett.* **5**, 173–180 (2016). <https://doi.org/10.5267/j.ccl.2016.7.001>
58. M. Tian et al., Facile synthesis of rod-like  $\text{TiO}_2$ -based composite loaded with g- $\text{C}_3\text{N}_4$  for efficient removal of high-chroma organic pollutants based on adsorption-photocatalysis mechanism. *Inorg. Chem. Commun.* **141**, 109517 (2022). <https://doi.org/10.1016/j.inoche.2022.109517>
59. I. Okeke, K. Agwu, A. Ubachukwu, M. Maaza, F. Ezema, Impact of Cu doping on ZnO nanoparticles phyto-chemically synthesized for improved antibacterial and photocatalytic activities. *J. Nanopart. Res.* **22**, 272 (2020)
60. A. Kumar Paul, G. Madras, S. Natarajan, Adsorption-desorption and photocatalytic properties of inorganic-organic hybrid cadmium thiosulfate compounds. *Phys. Chem. Chem. Phys.* **11**(47), 11285–11296 (2009). <https://doi.org/10.1039/b913407g>
61. E. Gao et al., Insights on the mechanism of enhanced selective catalytic reduction of NO with  $\text{NH}_3$  over Zr-doped  $\text{MnCr}_2\text{O}_4$ : A combination of in situ DRIFTS and DFT. *Chem. Eng. J* (2019). <https://doi.org/10.1016/j.cej.2019.123956>
62. S. Chiam, S. Pung, F. Yeoh, Recent developments in  $\text{MnO}_2$ -based photocatalysts for organic dye removal: a review. *Environ. Sci. Pollut Res.* (2020). <https://doi.org/10.1007/s11356-019-07568-8>
63. M.A. Rauf, S.S. Ashraf, Fundamental principles and application of heterogeneous photocatalytic degradation of dyes in solution. *Chem. Eng. J.* **151**, 1–3 (2009). <https://doi.org/10.1016/j.cej.2009.02.026>
64. C. Boon, L. Yong, A. Wahab, A review of ZnO nanoparticles as solar photocatalysts: synthesis, mechanisms and applications. *Renew. Sustain. Energy Rev.* **81**, 536–551 (2018). <https://doi.org/10.1016/j.rser.2017.08.020>
65. I.L. Ikhioya, C.O. Ugwuoke, D.N. Okoli, A.J. Ekpunobi, M. Maaza, F.I. Ezema, Effect of cobalt on the photovoltaic properties of zinc selenide thin film deposited on fluorine-doped tin oxide (FTO) via electrochemical deposition technique. *Curr. Res. Green. Sustain. Chem.* (2022). <https://doi.org/10.1016/j.cogsc.2022.100630>
66. W. Yuan, X. Liu, L. Li, Synthesis, characterization and photocatalytic activity of cubic-like  $\text{CuCr}_2\text{O}_4$  for dye degradation under visible light irradiation. *Appl. Surf. Sci.* (2014). <https://doi.org/10.1016/J.APSUSC.2014.07.158>
67. S. Taghavi Fardood et al., Facile green synthesis, characterization and visible light photocatalytic activity of  $\text{MgFe}_2\text{O}_4$ @ $\text{CoCr}_2\text{O}_4$  magnetic nanocomposite. *J. Photochem. Photobiol A Chem.* **423**, 3–5 (2022). <https://doi.org/10.1016/j.jphotochem.2021.113621>
68. P. de Cubas, A.W. Semkiw, F.C. Monteiro, P. Los Weinert, J.F.H.L. Monteiro, S.T. Fujiwara, Synthesis of  $\text{CuCr}_2\text{O}_4$  by self-combustion method and photocatalytic activity in the degradation of Azo Dye with visible light. *J. Photochem. Photobiol. A Chem* (2019). <https://doi.org/10.1016/j.jphotochem.2020.112797>
69. F. Beshkar, O. Amiri, M. Salavati-Niasari, F. Beshkar, Novel dendrite-like  $\text{CuCr}_2\text{O}_4$  photocatalyst prepared by a simple route in order to remove of azo dye in textile and dyeing wastewater. *J. Mater. Sci. Mater. Electron.* **26**(10), 8182–8192 (2015). <https://doi.org/10.1007/s10854-015-3479-0>
70. R. Bajaj, M. Sharma, D. Bahadur, Visible light-driven novel nanocomposite ( $\text{BiVO}_4$ / $\text{CuCr}_2\text{O}_4$ ) for efficient degradation of organic dye. *Dalt Trans.* **42**, 6736–6744 (2013). <https://doi.org/10.1039/c2dt32753h>

**Publisher's note** Springer Nature remains neutral with regard to jurisdictional claims in published maps and institutional affiliations.

Springer Nature or its licensor (e.g. a society or other partner) holds exclusive rights to this article under a publishing agreement with the author(s) or other rightsholder(s); author self-archiving of the accepted manuscript version of this article is solely governed by the terms of such publishing agreement and applicable law.